QUARTERLY JOURNAL OF THE ROYAL METEOROLOGICAL SOCIETY
Q. J. R. Meteorol. Soc. **133**: 1913–1931 (2007)
Published online in Wiley InterScience
(www.interscience.wiley.com) DOI: 10.1002/qj.172

Albedo, atmospheric solar absorption and heating rate measurements with stacked UAVs

M. V. Ramana,* V. Ramanathan, D. Kim, G. C. Roberts and C. E. Corrigan
Center for Atmospheric Sciences, Scripps Institution of Oceanography, University of California at San Diego, La Jolla, USA

ABSTRACT: This paper reports unique measurements of albedo, atmospheric solar absorption, and heating rates in the visible (0.4 to 0.7 μm) and broadband (0.3 to 2.8 μm) spectral regions using vertically stacked multiple lightweight autonomous unmanned aerial vehicles (UAVs). The most significant finding of this study is that when absorbing aerosols and water vapour concentrations are measured accurately and accounted for in models, and when heating rates are measured directly with stacked aircraft, the simulated clear sky heating rates are consistent with the observed broadband heating rates within experimental errors (about 15%). We conclude that there is no need to invoke anomalous or excess absorption or unknown physics in clear skies.

Aerosol–radiation–cloud measurements were made over the tropical Indian Ocean within the lowest 3 km of the atmosphere during the Maldives Autonomous UAV Campaign (MAC). The UAVs and ground-based remote sensing instruments determined most of the parameters required for calculating the albedo and vertical distribution of solar fluxes. The paper provides a refined analytical procedure to reduce errors and biases due to the offset errors arising from mounting of the radiometers on the aircraft and due to the aircraft attitude. Measured fluxes have been compared with those derived from a Monte-Carlo radiative transfer algorithm which can incorporate both gaseous and aerosol components. Under cloud-free conditions the calculated and measured incoming fluxes agree within 2–10 W m^{-2} (<1%) depending upon the altitudes. Similarly, the measured and calculated reflected fluxes agreed within 2–5 W m^{-2} (<5%).

The analysis focuses on a cloud-free day when the air was polluted due to long-range transport from India, and the mean aerosol optical depth (AOD) was 0.31 and mean single scattering albedo was 0.92. The UAV-measured absorption AOD was 0.019 which agreed within 20% of the value of 0.024 reported by a ground-based instrument. The observed and simulated solar absorption agreed within 5% above 1.0 km and aerosol absorption accounted for 30% to 50% of the absorption depending upon the altitude and solar zenith angle. Thus there was no need to invoke spurious or anomalous absorption, provided we accounted for aerosol black carbon. The diurnal mean absorption values for altitudes between 0.5 and 3.0 km above mean sea level were observed to be 41 ± 3 W m^{-2} (1.5 K/day) in the broadband region and 8 ± 2 W m^{-2} (0.3 K/day) in the visible region. The contribution of absorbing aerosols to the heating rate was an order of magnitude larger than the contribution of CO_2 and one-third that of the water vapour. In the lowest 3 km of the tropical atmosphere, aerosols accounted for more than 80% of the atmospheric absorption in the visible region. Copyright © 2007 Royal Meteorological Society

KEY WORDS aircraft measurements; aerosol optical properties; anomalous absorption

Received 20 March 2007; Revised 27 July 2007; Accepted 18 September 2007

1. Introduction

One of the major uncertainties in our understanding of the planetary radiation budget concerns the absorption of solar radiation within the atmosphere (Ramanathan and Vogelmann 1997). More than two decades of satellite radiation budget measurements (Wielicki *et al*., 1995) have constrained the planetary albedo to be 29% (±2%). On the other hand, our estimates of global mean solar absorption ranges from 20% to 28% (Ramanathan and Vogelmann, 1997). The lower value of 20% is mostly derived by general circulation climate models (e.g. Kiehl and Trenberth, 1997), whereas the upper value of 28% was estimated by combining over 1000 land-based surface radiometric observations with satellite estimates of albedo (Ohmura and Gilgen, 1993). Neither of these approaches (models or observationally constrained) can be assumed to be closer to reality. Models, generally, lack some basic parameters such as vertical distribution of absorbing aerosols, and microphysical parameters of clouds, particularly for ice phase clouds, among numerous others. Observationally-based approaches (e.g. Ohmura and Gilgen, 1993) lack adequate spatial coverage over the oceans and are unable to reliably account for the scale mismatch between satellite observations of albedo and surface-based radiometric data. It has been a great challenge to measure both albedo and absorption simultaneously in cloudy and hazy atmospheres since it requires multiple aircraft to determine albedo, cloud, and aerosol properties along with radiation fluxes measured

* Correspondence to: M. V. Ramana, Center for Atmospheric Sciences, Scripps Institute of Oceanography, 9500 Gilman Drive, La Jolla, CA 92093-0221, USA. E-mail: ramana@fiji.ucsd.edu

at different levels to determine the atmospheric solar absorption.

During the last few decades several attempts have been made to determine atmospheric solar absorption directly from radiometric observations and to simulate the measurements with models. In general, model simulations have typically underestimated the solar absorption with respect to observations and this discrepancy has been termed anomalous absorption (Stephens and Tsay, 1990) or excess solar absorption (Ramanathan and Vogelmann, 1997). Following Ramanathan and Vogelmann (1997), we will refer to the positive difference between the 'observed' and the simulated absorption as *excess absorption*, and refer to the controversy or debate surrounding this issue as *anomalous absorption*. Using aircraft data, inconsistencies between simulated and observed solar absorption in cloudy skies were revealed as early as the1950s (e.g. Fritz, 1951; see review of the earlier studies in Stephens and Tsay, 1990). The excess solar absorption issue became a major focus of research after the publication of three observational studies, all in 1995 (Cess *et al*., 1995; Pilewskie and Valero, 1995; Ramanathan *et al*., 1995). These three studies did not find significant discrepancy in the clear skies, but suggested significant excess absorption in cloudy atmospheres (15–35 W m^{-2} diurnal average), thus supporting the earlier aircraft data. The Ramanathan *et al*. and Pilewski and Valero studies were restricted to the western Pacific warm pool region. The Cess *et al*. study, on the other hand, suggested that the excess solar absorption is a global-scale phenomenon and thus was challenged by several publications (see the review in Ramanathan and Vogelmann, 1997).

Motivated by the importance of the problem, the Atmospheric Radiation Measurement (ARM) programme initiated two aircraft studies, referred to as the Atmospheric Radiation Measurement (ARM) Enhanced Shortwave Experiment (ARESE) over north central Oklahoma during autumn 1995 (Valero *et al*., 1997a, 1997b): two aircraft flew simultaneously above and below the clouds to try and quantify the amount of absorption associated with the clouds. The ARESE data were used by one group of studies (Valero *et al*., 1997a, 1997b; Zender *et al*., 1997; Arking, 1999; Cess *et al*., 1999) to conclude that the observations showed very large deviations from existing radiative transfer models for heavy overcast days, while another study (Li *et al*., 1999) suggested that the observed solar absorption in cloudy skies is consistent with observations (within experimental errors). A follow-up campaign, ARESE II, was conducted over the Oklahoma ARM site in 2000 using one aircraft and surface measurements. Several papers (Ackerman *et al*., 2003; O'Hirok and Gautier, 2003; Oreopoulos *et al*., 2003; Valero *et al*., 2003) discussed the results of ARESE II and concluded that the extreme anomalous absorption observed in earlier studies was not detected, but the studies could not arrive at a definitive answer regarding the existence, or the lack, of anomalous absorption.

Observations collected during other field campaigns have also not shown evidence of strong excess absorption in cloudy skies. For example, although Francis *et al*. (1997) reported aircraft experiments that showed measured cloud absorptions greater than values predicted by models, the discrepancies were much smaller than those suggested in previous studies. Asano *et al*. (2000) analysed collocated aircraft measurements of marine stratocumulus and radiative fluxes made in 1998 over the Sea of Japan and found no evidence of excess solar absorption from clouds. One limitation of all of these field studies is that they are restricted to low-level water clouds, whereas the empirical studies that were suggesting strong excess solar absorption (Cess *et al*., 1995; Pilewski and Valero, 1995; Ramanathan *et al*., 1995) included low as well as mid-level and high clouds.

The anomalous absorption controversy also exists for clear-sky solar absorption. Arking (1996) used satellite observations to conclude that observationally estimated clear-sky absorption values exceed those predicted by models. Similar conclusions were reached by others (e.g. Kato *et al*., 1997; Halthore *et al*., 1998) based on analyses of a large database from the Oklahoma ARM site. Conversely, Zender *et al*. (1997) and Jing and Cess (1998), using ARM data, did not find excess atmospheric absorption in clear skies beyond the uncertainties in the model and observations.

Clearly, there is a great need for more comprehensive experiments that can clarify the issue and reduce the uncertainty in the atmospheric solar absorption. A fundamental limitation of the earlier studies on solar absorption was that these studies did not have access to multiple aircraft flux measurements throughout the vertical column. Typically, a minimum of three identical or nearly identical (similar air speed, wing span etc.) aircraft are required: two to measure the solar fluxes at two different levels (to determine flux divergence) and one to measure the in-cloud properties. The key criterion is that all three aircraft should be flying over the same spot and within tens of seconds to avoid ambiguities that arise from spatial and temporal variability in aerosols and clouds. A second limitation was that the earlier experiments did not measure aerosol, particularly black carbon, simultaneous with solar flux measurements and thus could not accurately estimate the contribution of aerosols to albedo and to solar absorption. These limitations were recently overcome during the Maldives Autonomous Unmanned Aerial Vehicle (UAV) Campaign (MAC), where 3 lightweight UAVs (<30 kg) flew in a coordinated formation stacked vertically between 0.5 and 3.0 km altitude over the Indian Ocean (Ramanathan *et al*., 2007). The UAVs were equipped with miniaturized instruments for measuring aerosol number concentration, mass of black carbon, cloud drop number density as a function of radius, water vapour distribution, and incoming as well as outgoing solar fluxes at both broadband and narrow band wavelengths. In addition, surface-based measurements were made (within a few kilometres of the flight domain) to determine column-integrated values of

DOI: 10.1002/qj

ozone, water vapour, aerosol extinction and absorption optical depth at four solar wavelengths.

The primary focus of this paper is on clear-sky solar absorption. The cloudy-sky solar absorption data collected during MAC will be the subject of a follow-up study. This paper focuses on a cloud-free day and examines the closure between measured and simulated atmospheric solar absorption and heating rates.

2. Description of observations

2.1. MAC

The MAC campaign took place from 6 March to 31 March 2006 over the northern Indian Ocean off the coast of Hanimaadhoo (6.776 °N, 73.183 °E), Maldives. During the MAC campaign 18 different scientific missions were flown by aircraft equipped with aerosol, radiation and cloud instruments. The science missions consisted of primary stacked missions involving three Autonomous UAV (AUAV) platforms (10 such missions were flown); alternate missions with two platforms (7 missions); and a single-platform mission. In the three-AUAV stacked flight configuration, aircraft flew below the clouds (BC), in-cloud (IC), and above the clouds (AC) which enabled the simultaneous measurements of aerosols, black carbon, cloud microphysics and solar radiation fluxes from different points surrounding the clouds. The alternate science missions enabled the comparison and validation of measurements, vertical profiling of black carbon and aerosol, and the measurements of aerosol and cloud absorption. During ascent and descent, and at various times throughout the mission, vertical profiles of aerosol parameters were obtained. In general, the IC and AC platforms sampled between 0.65 and 1.0 km and 2.0–3.0 km above mean sea level (a.m.s.l.), respectively. The BC platform typically flew ∼50–100 m below the cloud system and on some missions sampled within the pollution layer at 1.5 km a.m.s.l. for the second half of the flight. The aircraft followed pre-generated flight paths that consisted of flying back and forth along a 5–10 km line at constant altitudes. The flight paths were maintained at an angle of greater than 30° to the prevailing wind to avoid sampling of the aircraft exhaust plume. In addition, special turning paths (90°–270° turns) were incorporated based on prevailing wind direction to avoid sampling of aircraft plumes during turns. The autopilot software in the ground station maintained the three aircraft in stacked formation such that all aircraft usually passed over the same geographic point within 10 s of each other (within 3 s 75% of the time).

A list of miniaturized instruments installed onboard the UAVs during the MAC experiment is given in Table I. Aerosol, cloud and radiometric instrumentation along with an integrated data acquisition system were miniaturized to achieve a total payload weight less than 5 kg and a power requirement less than 50 W. The Kipp & Zonen CM 21 pyranometer and the Li-Cor Li-190 quantum sensor (also called the 'Photo-synthetically Active Radiation' or PAR sensor) are used to measure the incoming and reflected solar radiation in the broadband (0.3–2.8 μm) and visible (0.4–0.7 μm) spectral ranges, respectively. We have reduced the size and weight of the

Table I. Instrumentation carried onboard UAVs during the MAC experiment.

Instrument	Above cloud (AC)	In-Cloud (IC)	Below-Cloud (BC)
Aerosol:			
Total concentrations (CPC; >0.01 μm)	Installed		Installed
Size distribution (OPC; 0.3 – 3.0 μm)	Installed		Installed
Absorption Coeff (Aethalometer; 370, 520, and 880 nm)	Installed		Installed
Aerosol inlet + flow splitter + cyclone	Installed		Installed
Radiation:			
Up/Down broadband fluxes (Pyranometer; 0.3–2.8 μm)	Installed		Installed
Up/Down visible fluxes (PAR; 0.4–0.7 μm)	Installed		Installed
Clouds:			
Drop size distribution (CDP;1–50 μm)		Installed	
Liquid water content probe (LWC)		Installed	
Video camera + downlink		Installed	
Turbulence:			
Gust probe		Installed	
Meteorological (T, RH, P)	Installed	Installed	Installed
Data Acquisition system	Installed	Installed	Installed
Batteries + Miscellaneous	Installed	Installed	Installed
Total weight	5.4 Kg	5.3 Kg	3.9 Kg

CPC: Condensation Particle Counter; OPC: Optical Particle Counter; CDP: Cloud Droplet Probe;
PAR: Photo-synthetically Active Radiation; T: Air Temperature; RH: Relative Humidity; P: Atmospheric Pressure

DOI: 10.1002/qj

pyranometer mounting structures and added an amplified circuit and temperature probe. The PAR sensor also received an amplified circuit. These instruments were modified in such a way that the quality of the data was not lost after the miniaturization process. Pyranometers and PARs were mounted on the top and bottom of the fuselage of aerosol–radiation platforms (AC and BC) such that the sensors had the best possible view of their respective hemispheres (see Figure 1(a)). A venting system was incorporated into the aircraft fuselage to allow the ambient air to pass by the underside of the pyranometer to maintain thermal equilibrium throughout the entire sensor housing (see Figure 1(b)). All measurements had a sampling rate of 1 Hz and the missions typically lasted 3–4 hours.

MAC data were compared with surface measurements using identical instruments to those flown onboard the UAVs. Ground-based measurements were acquired at the Maldives Climate Observatory in Hanimaadhoo (MCOH) (Corrigan *et al*., 2006; Ramana and Ramanathan, 2006). The MCOH facility contains a set of radiometers covering the spectrum from the near ultraviolet to the far infrared (Ramana and Ramanathan, 2006) and aerosol instruments that perform physical, optical and chemical measurements (Corrigan *et al*., 2006). Ramana and Ramanathan (2006) have assessed the precision of the MCOH radiometers and have used these flux measurements to validate the Monte Carlo radiative transfer model (see Appendix B for model description) used in this study. The surface insolation in the broadband and visible regions at MCOH was measured respectively by an upward facing pyranometer (Kipp & Zonen CM 21) and a narrow-band radiometer (Bio-spherical Instruments GUV-2511) that were similar to the instruments flown on the UAVs. The spectral aerosol optical depth (AOD), columnar single scattering albedo (SSA), and columnar precipitable water vapour (PWV) were measured using the CIMEL sunphotometer (Holben *et al*., 1998; Dubovik *et al*., 2000) operating at MCOH.

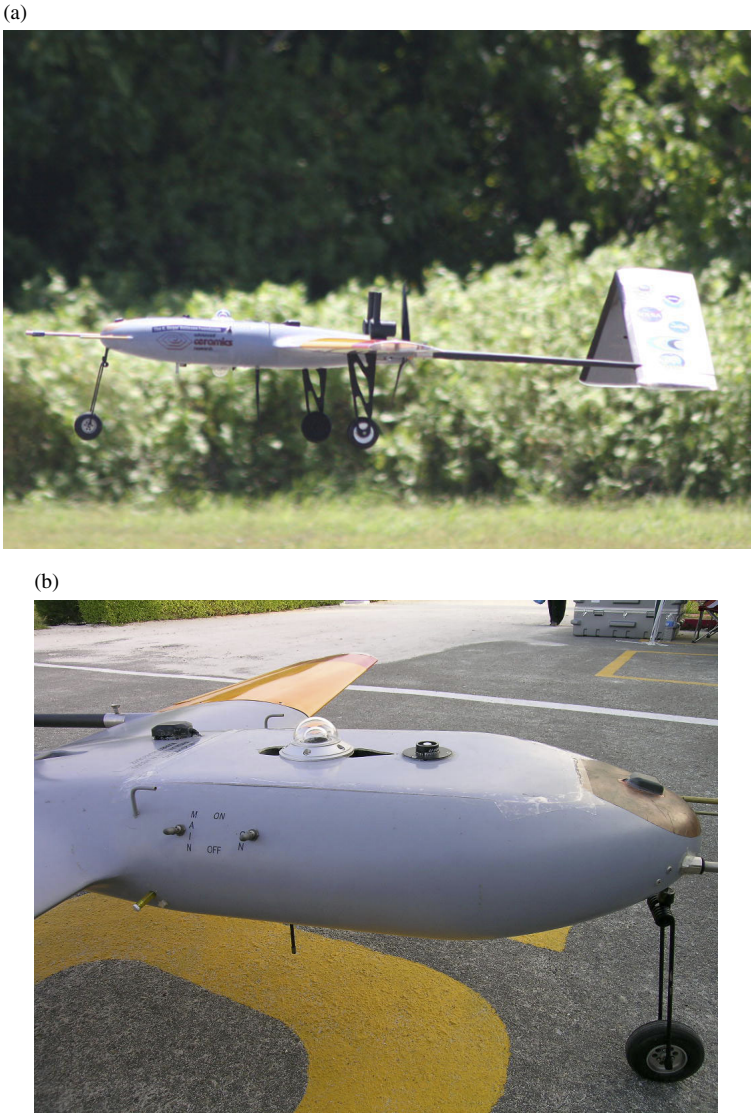

Figure 1. (a) Photo of the autonomous UAV showing the radiation instruments on the top and bottom of the aircrafts fuselage; and (b) view of the top radiometers with venting ports fore and aft of the pyranometer. This figure is available in colour online at www.interscience.wiley.com/qj

DOI: 10.1002/qj

2.2. Data reduction

Measuring radiation fluxes using a moving airborne platform presents challenges due to changes in the radiometers' fields of view as the aircraft attitude varies. Several steps were adopted to infer the attitude-corrected irradiances from the measured MAC radiation data and these post-flight correction techniques are explained in detail in Appendix A. The corrections included time response adjustments to the measured fluxes as well as pitch–roll and mounting offset errors to the direct component of the downward flux. Figure 2(a) and (b) show the observed incoming fluxes at 3 km altitude in the broadband and visible spectral regions on 24 March. The systematic oscillations between inbound and outbound flight tracks were due to sensor mounting offsets with respect to the UAV navigation reference coordinate system, and the variability within each track was due to changes in aircraft pitch and roll. The data were corrected for these errors using the method described in Appendix A. The corrected broadband and visible incoming fluxes at 3 km altitude for the 24 March flight are shown in Figure 2(c) and (d). The corrected fluxes show a significant reduction in the systematic difference between the inbound and the outbound tracks. In order to further reduce the uncertainties, we only use the data when the aircraft was performing a nearly level flight (i.e. less than ±2 deg of pitch–roll). The averaged data for each pair of inbound and outbound tracks were used to calculate albedo, atmospheric absorption and atmospheric heating rates.

3. Description of simulations: MACR

Incoming and reflected fluxes for the atmospheric conditions representative of the flight missions were simulated using the three-dimensional Monte-Carlo Aerosol Cloud Radiation (MACR) photon transport radiative transfer algorithm described in Appendix B (Podgorny *et al*. 2000; Podgorny and Ramanathan, 2001; Vogelmann *et al*., 2001). MACR has been validated (Ramana and Ramanathan, 2006) with observed surface solar fluxes at MCOH. The simulated values agreed with measured fluxes within instrumental uncertainties (2–5 W m^{-2}).

For MAC, observed aerosol properties collected at the surface (by sunphotometers) and at altitude using aircraft were used as input parameters for the MACR calculations. The measured column-integrated input parameters (aerosol optical properties, water vapour, ozone) for the MACR calculations specific to 29 March are given in Appendix B. In addition, the vertical profiles from MAC were incorporated into MACR using the following procedure. AOD vertical profiles were obtained by scaling the MAC-measured aerosol number concentration vertical profile with column-integrated AOD measurements from the CIMEL sunphotometer. AOD for each layer was determined using the following equation:

$$AOD_l = \frac{\overline{CPC_l}\cdot\Delta z}{\sum_{l=0}^{3km}\overline{CPC_l}\cdot\Delta z}\cdot AOD_{\text{columnar}} \qquad (1)$$

where AOD_l is aerosol optical depth for a layer l, CPC_l is aerosol number concentration (cm^{-3}) for layer

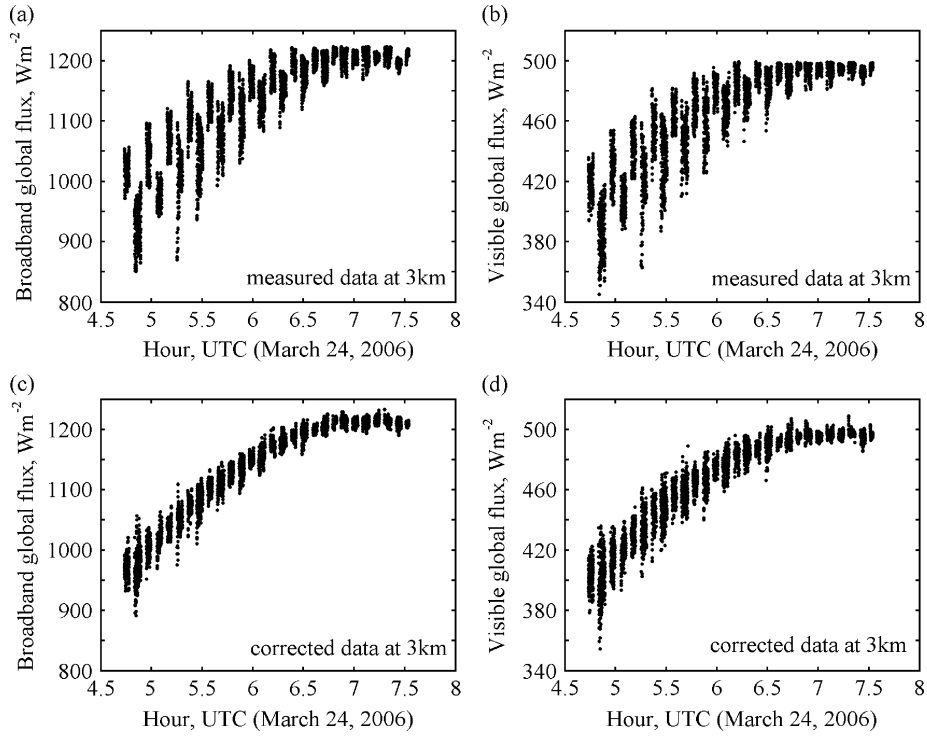

Figure 2. Measured (a) broadband (0.3–2.8 μm) and (b) visible (0.4–0.7 μm) fluxes at 3 km altitude on 24 March 2006. Aircraft attitude and mounting offset corrected fluxes in the (c) broadband and (d) visible spectral region at 3 km altitude on 24 March.

DOI: 10.1002/qj

l, AOD_{columnar} is columnar (total) AOD, and Δz is the thickness of the layer l. If the aerosol number concentration vertical profiles indicate more than 100 particles/cm^3 at 3 km altitude, then the AOD was assumed to decrease exponentially above 3 km. The deduced AOD vertical profile along with the vertical distribution of aerosol number concentration measured (with a miniaturized condensation particle counter) during the aircraft profile on 29 March are shown in Figure 3(a). The vertical resolution of the MACR within the troposphere is 0.5 km and hence the measured vertical parameters are averaged in 0.5 km altitude steps.

Similarly, the columnar SSA measured using the CIMEL sunphotometer was scaled with MAC-measured aerosol absorption coefficient profiles to yield SSA altitude profiles. The SSA for each layer was determined using the following equations:

$$SSA_l = 1 - \frac{AOD_l^{\text{abs}}}{AOD_l} \quad \text{from surface to 3 km} \quad (2)$$

$$SSA_l = 1 \quad \text{from 3 km to TOA} \quad (3)$$

$$AOD_l^{\text{abs}} = \frac{\overline{BC_l} \cdot \Delta z}{\sum_{l=0}^{3km} \overline{BC_l} \cdot \Delta z} \cdot AOD_{\text{col}} \cdot (1 - SSA_{\text{col}}) \quad (4)$$

where SSA_l is SSA for a layer l, AOD_l^{abs} is absorption optical depth for layer l, BC_l is absorption coefficient (Mm^{-1}) for layer l, AOD_{col} is columnar AOD, SSA_{col} is columnar SSA, and Δz is the thickness of the layer l. The deduced SSA vertical profile and the vertical distribution of aerosol absorption coefficient (Mm^{-1}) measured (with miniaturized absorption photometer) during the aircraft profile on 29 March are shown in Figure 3(b).

Measured vertical profiles of pressure, temperature and water vapour concentration from the MAC experiment were used in the MACR calculations (shown in Figure 3(c)). Profile information above the maximum MAC measurement altitude (>3 km altitude) was taken from the tropical standard atmosphere (McClatchey *et al.*, 1971). The amount of water vapour above 3 km was obtained by subtracting the surface to 3 km integrated PWV value (MAC measurements) from the measured

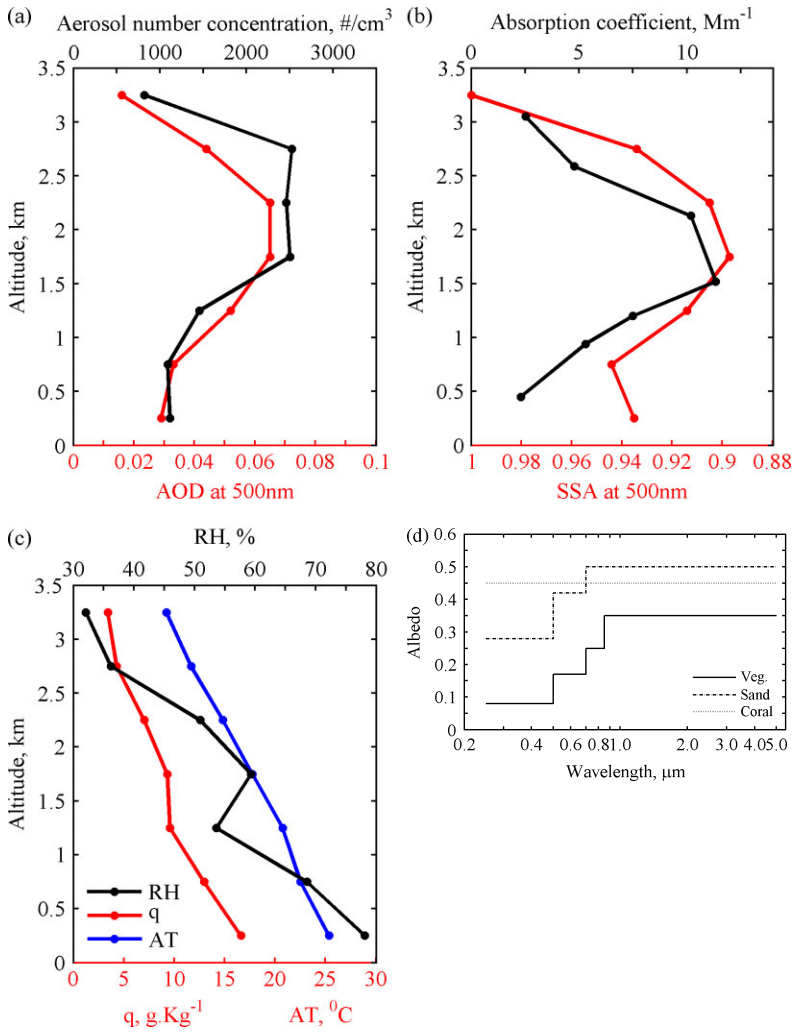

Figure 3. Measured vertical profiles of (a) aerosol concentration and aerosol optical depth (AOD); (b) absorption coefficient and single scattering albedo (SSA); (c) relative humidity (RH), air temperature (AT), and humidity mixing ratio (q), on 29 March, and (d) spectral dependence of surface albedo for each surface type used in MACR. This figure is available in colour online at www.interscience.wiley.com/qj

DOI: 10.1002/qj

columnar PWV value (CIMEL sunphotometer). Columnar ozone concentration measured using a hand-held Microtops sunphotometer was used to scale the tropical standard ozone profile so that it agreed with the measurements. The reflected flux calculations accounted for the horizontal variations in surface albedos introduced by the island within the oceanic domain. The surface albedo inhomogeneities were treated with Hanimaadhoo island at the centre of the domain (12 km by 12 km with 120 m resolution) surrounding by open ocean. The zenith-angle-dependent ocean surface albedo, and spectral-dependent vegetation and sand albedos were taken from Breigleb *et al*. (1986). Shallow waters in the extended reef were treated differently from open ocean since the coral sand bottom in shallow waters reflects a significant amount of the incoming solar radiation. The albedo of the coral reef surrounding the island was assumed to be 0.45 in the short-wave range. Figure 3(d) shows the spectral dependence of surface albedo for each surface type (vegetation, sand and coral) incorporated into the MACR. As shown later, the ultimate test of these parametrizations are UAV measurements of albedo as a function of altitude.

4. Validation of observations and simulations

4.1. Validation of UAV radiometers with surface measurements

MAC miniaturized radiometers (8 pyranometers and 6 PARs) were first calibrated against MCOH radiometers before the campaign began. The MAC radiometers were observed to be within $\pm 0.5\%$ for all the miniaturized sensors, and it was concluded that the radiation values obtained with the miniaturized radiometers must be accurate within ± 1–2%, as stated by the manufacturer for the diurnal means. Several times during the MAC experiment, the flight radiation instruments were compared with MCOH upward-facing radiometers, and always agreed to better than $\pm 0.5\%$. Moreover, a mission comparing measurements from two aircraft flying side by side was performed to ensure reproducibility across platforms (discussed in Section 4.2). The response times of the pyranometer and PAR are 3 s and 1 s, respectively (see Appendix A). In general, all UAV-mounted instruments functioned satisfactorily throughout the MAC experiment.

4.2. Validation of airborne radiometers by wing tip to wing tip comparisons

Since our study used more than one aircraft to measure the solar flux divergence, inter-aircraft comparisons were performed to test the precision of the airborne radiometric measurements. By having the aircraft fly in formation at the same altitude within a few kilometres of each other, we were able to determine the uncertainties of airborne radiometers. On 28 March, AC and BC platforms were flown in the east–west plane at the same altitude (within ± 100 m) along parallel flight paths separated by 1 km. Both the platforms were flown at 1.5, 2.5 and 3.0 km altitudes for about 45 minutes at each level along an 11 km flight path. Figure 4 compares broadband and visible fluxes (AC_incoming vs. BC_incoming and AC_reflected vs. BC_reflected). Each point in the figure represents the track mean value. The mean differences in the incoming solar radiation measured by the two UAVs are within 4.6 W m^{-2} (0.5%) and 3.2 W m^{-2} (0.8%), respectively in the broadband and visible spectral regions. For the reflected flux, the corresponding differences are within 2.6 W m^{-2} (2%) and 0.9 W m^{-2} (2%). These differences are consistent with the instrumental uncertainties ($\pm 2\%$) measured at the ground in MCOH which suggest that no additional errors were introduced when the radiometers were installed in the UAVs.

4.3. Validation of simulated fluxes

Thus far we have quantified the uncertainties in the fluxes determined by the UAVs. The next step is to quantify the uncertainties in the simulated fluxes by comparing with airborne data. Comparisons were carried out using 29 March two-track (in- and out-bound) average data. The 29 March data were used mainly because the AC and BC platforms were flown at multiple altitudes under cloud-free conditions. Figures 5 and 6 compare the measured with the simulated visible and broadband incoming fluxes at different altitudes. The comparison of incoming fluxes at multiple altitudes shows that the calculated fluxes were within 5 and 10 W m^{-2} (1%) of the measured fluxes for visible global and broadband fluxes, respectively. The reflected fluxes provide a more critical test for the MACR prescription of the spatial and spectral inhomogeneities in surface albedo. Figure 7(a) and (b) compare reflected fluxes. The simulated fluxes are within 2 and 5 W m^{-2} (5%) of the measured fluxes for the visible and broadband regions, respectively. The mean differences shown in Figures 5 to 7 are well within the instrumental errors of about 2%. Furthermore they are also within the uncertainties in the airborne radiometers estimated earlier.

4.4. Uncertainties in measured and simulated solar absorption

The manufacturer's stated accuracy for the radiometers is $\pm 2\%$. However, the MAC radiometers agreed to within $\pm 0.5\%$. The airborne MAC pyranometers were able to determine the incoming solar fluxes to within 4.6 W m^{-2} and the reflected solar fluxes to within 2.6 W m^{-2} (Figure 4). The corresponding uncertainties in PAR are within 3 and 1 W m^{-2}. Basically, the atmospheric solar absorption is the difference between the incoming and reflected solar fluxes at two different levels and we assume the errors in each of the measured fluxes are uncorrelated. Thus the cumulative error in the estimated atmospheric solar absorption is the square root of the sum of the squares of the individual errors due to the four radiometers. The resulting error in the estimated

DOI: 10.1002/qj

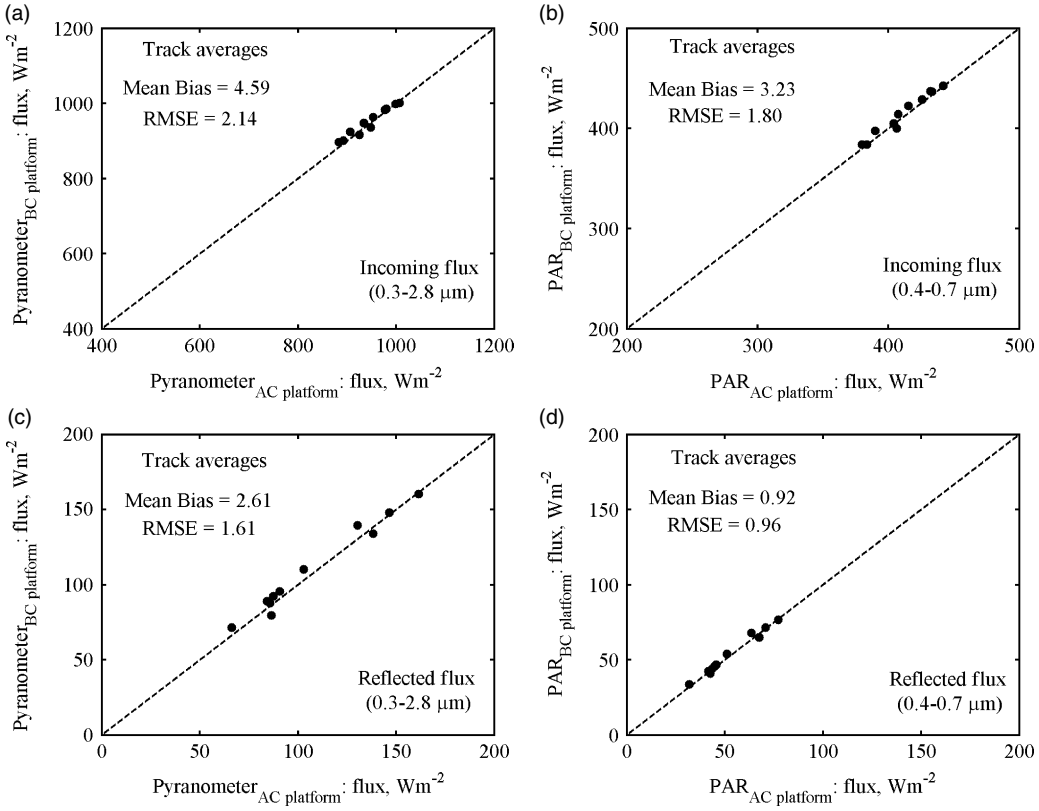

Figure 4. Wing tip to wing tip comparison of aerosol–radiation platforms (AC vs. BC) for (a) incoming broadband global fluxes (0.3–2.8 μm), (b) incoming visible global fluxes (0.4–0.7 μm), (c) reflected fluxes in the broadband region, and (d) reflected fluxes in the visible region. The dashed line corresponds to perfect agreement.

atmospheric solar absorption is ±7.5 W m^{-2} (±8%) in the broadband region and ±4.7 W m^{-2} (±25%) in the visible region.

The uncertainties in MACR calculations arise from accuracies in the airborne measurements of parameters used as input to MACR and from the use of assumed standard profiles above the lower troposphere (>3 km). Another source of error is uncertainties in column-integrated input parameters, namely, uncertainties in AOD, SSA, PWV and ozone. The largest potential error arises primarily from uncertainties in the PWV. The error in the water vapour column amount is conservatively estimated to be 10%. Applying this to the measurement gives a total water column of 3.15 ± 0.3 cm, giving an uncertainty of 2.2 W m^{-2} (5.5%) in the broadband solar absorption. The uncertainties in MACR-calculated solar absorption values associated with various input parameters are given in Table II. We assume the sources of the individual errors are uncorrelated, and with this assumption, the maximum absolute error in the broadband solar absorption is about 7.5 W m^{-2} (18%) and the maximum error in the visible region is about 2.6 W m^{-2} (23%) between 0 and 3 km altitude over the diurnal means. These uncertainty estimates for the observed and simulated absorption are used in the subsequent analyses.

5. Results

5.1. Evolution of the aerosol optics during the campaign

Figure 8(a) and (b) show the temporal variation of AOD at 500 nm and PWV during March 2006 at MCOH measured using the CIMEL sunphotometer. The days when the AUAVs were flown are marked along the *x*-axis. Figure 8(a) reveals the large build-up of aerosols during the MAC experiment. The AOD was less than 0.2 until 14 March. It then varied between 0.2 and 0.5 during the remainder of March. The steep increase in AOD from 0.2 to 0.5 is due to the long-range transport of aerosols from continental sources. The columnar atmospheric water vapour content (Figure 8(b)) decreased from a value of 4.5 cm during the beginning of the campaign to 3–3.5 cm as the campaign progressed. The columnar single scattering albedo (SSA) during March 2006 is in the 0.85 to 0.98 range, which suggests the presence of highly absorbing aerosols. Using the MAC experimental data, Corrigan *et al*. (2007) showed the altitude profiles of black carbon, aerosol number concentrations, aerosol size distribution, and the evolution of aerosol layers with altitude throughout the campaign. The majority of the aerosol was confined within the boundary layer at the beginning of the campaign, but after 19 March the largest concentration of aerosols was observed between 1.5 and

DOI: 10.1002/qj

2.5 km a.m.s.l. through to the end of the experiment (Ramanathan *et al*., 2007).

Wind back-trajectory analyses at multiple altitudes were used to identify the origin of aerosols arriving at the Maldives (Ramanathan *et al*., 2007). In general, 5-day back trajectory analysis up to 19 March indicates that the air mass originated primarily from marine sources. From 20 March onwards, 5-day back-trajectory analyses show that winds within the boundary layer were of marine origin and the higher level winds originated from south Asia and the Arabian Peninsula.

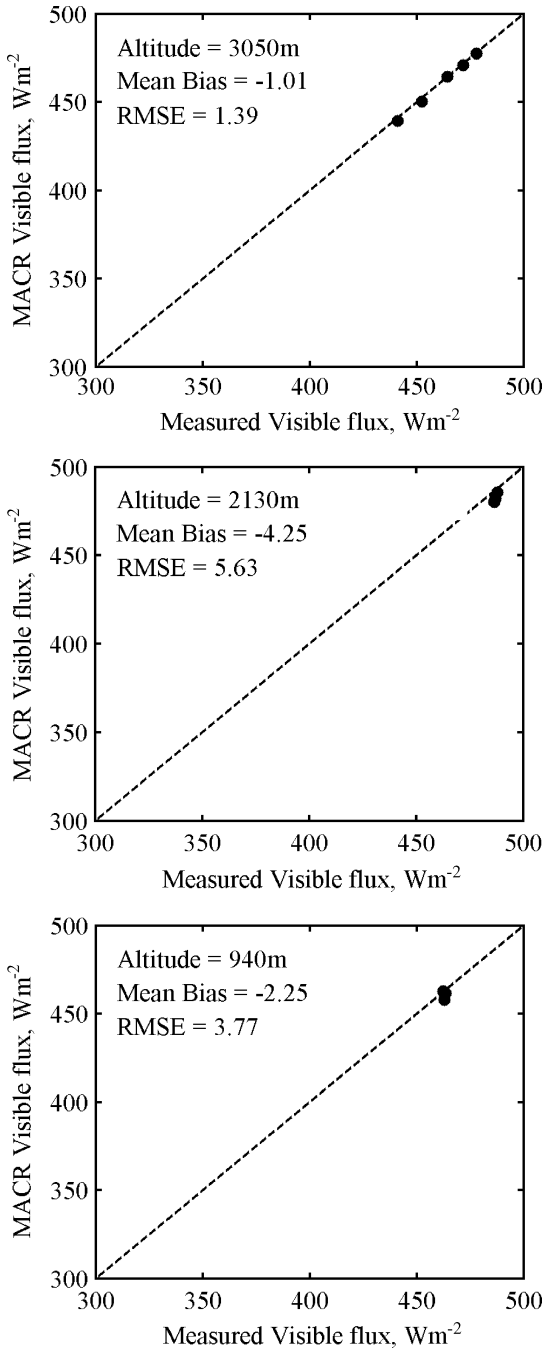

Figure 5. Measured versus MACR-calculated incoming visible (0.4–0.7 μm) fluxes at multiple altitudes. The dashed line corresponds to perfect agreement.

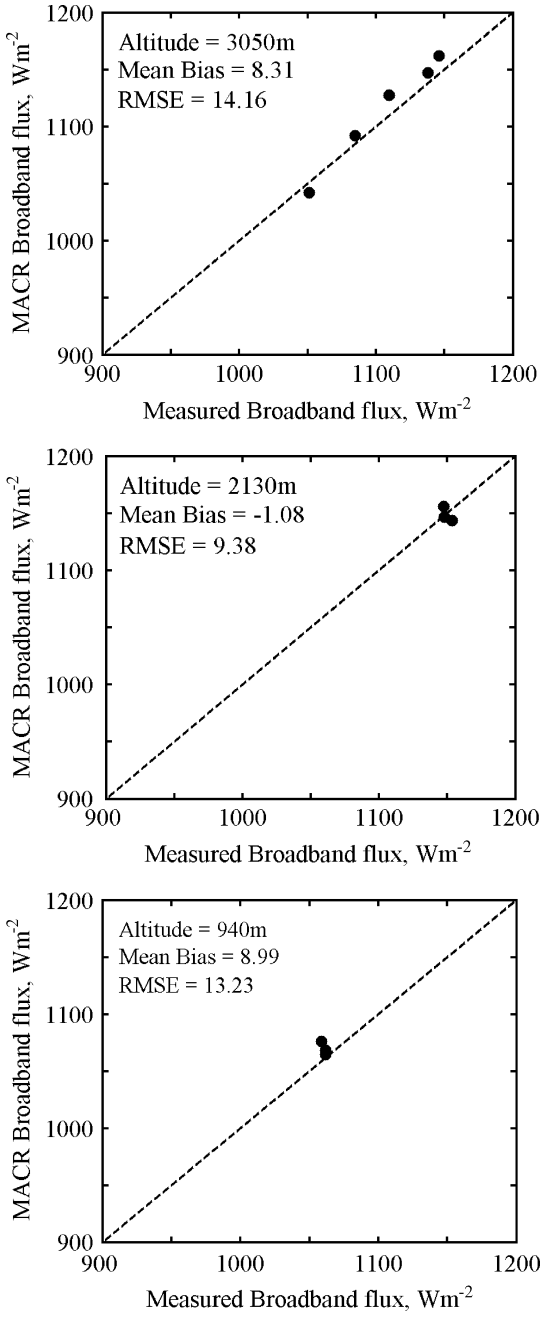

Figure 6. Measured versus MACR-calculated incoming broadband (0.3–2.8 μm) fluxes at multiple altitudes. The dashed line corresponds to perfect agreement.

5.2. Vertical variation of albedo

The albedo is the ratio of the amount of reflected solar radiation to the incoming solar radiation for any altitude. The broadband and visible albedo at 0.5, 1.5 and 3.0 km are calculated using simultaneous measurements of upward (reflected) and downward (incoming) fluxes. Figure 9 shows the broadband and visible albedos as a function of solar zenith angle for days that were low in cloud fraction (<5–10%). Each day's data is plotted with a different coloured symbol, and the number of individual cloud elements sampled (i.e. number of distinct clouds that the aircraft pass through) simultaneously with

DOI: 10.1002/qj

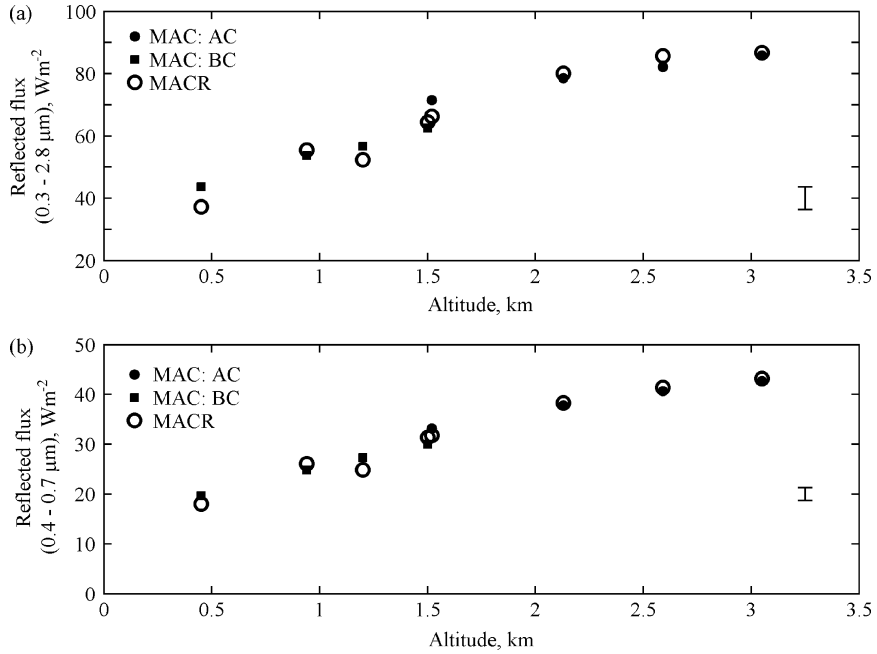

Figure 7. Measured versus MACR-calculated reflected fluxes in the (a) broadband region and (b) visible region at multiple altitudes.

Table II. The model uncertainties in the calculation solar absorption between 0 and 3 km altitude in the broadband and visible spectral regions due to input parameter uncertainties over the diurnal means.

Parameter (Uncertainty)	Broadband absorption, W m^{-2} (0–3 km altitude)	Visible absorption, W m^{-2} (0–3 km altitude)
AOD (±0.02)	0.96 (2.42%)	0.51 (4.75%)
SSA (±0.03)	4.56 (11.52%)	1.54 (14.25%)
Asy (±0.03)	0.03 (0.07%)	0.04 (0.34%)
PWV (10%)	2.19 (5.53%)	0.033 (0.31%)
Ozone (10%)	0.05 (0.12%)	0.023 (0.21%)
AOD profile (30% in aerosol profile)	0.17 (0.44%)	0.07 (0.67%)
SSA profile (30% in absorption profile)	4.88 (12.31%)	1.70 (15.68%)
PWV profile (10% in RH)	1.04 (3.6%)	0.032 (0.30%)
Albedo	0.03 (0.07%)	0.036 (0.33%)
Three-dimensional	2.0 (4.41%)	1.0 (13.89%)
Cumulative error	7.45* (18.78%)	2.56* (23.61%)

AOD: Aerosol Optical Depth; SSA: Single Scattering Albedo; Asy: Asymmetry parameter; PWV: Precipitable Water Vapour; RH: Relative Humidity

* Assumed that the individual errors are uncorrelated.

the in-cloud platform is given in the legend. In general, the albedo increases with the solar zenith angle for all altitudes. The broadband and visible albedos at all altitudes are highly correlated ($r \geq 0.96$) which is reassuring since it reveals the consistency between two independent instruments. The solid and dotted lines in Figure 9 show the simulated albedo for aerosol and aerosol-free atmospheres, respectively. Again it is reassuring that inclusion of aerosols brings the simulated values closer to the observed values. MACR calculations are performed for 29 March (cloud-free day) at the mean position of the flight track (6.741 °N, 73.19 °E).

The steep increase of albedo with zenith angle is mostly due to the zenith angle dependence of sea surface albedo, aerosol scattering and cloud albedo. The steeper slope on some cloudy days (e.g. see the cross symbols for 23 March) could also be due to the cloud-edge effects and three-dimensional cloud effects on reflected fluxes. The visible albedos are slightly higher than broadband albedos at 3.0 km altitude whereas the broadband albedos are slightly higher at lower altitude (0.5 km). This reversal arises because the spectral albedo of the inhomogeneous surface is slightly larger in the near-infrared region with respect to the visible region (see Figure 3(d)). With altitude, the near-infrared albedo decreases mainly due to absorption by water vapour; while the visible albedo increases due to scattering by air molecules and aerosols.

5.3. Solar absorption: Closure between measured and simulated values

We restrict this discussion only to clear sky conditions. Only on 29 March did clear skies persist throughout the

DOI: 10.1002/qj

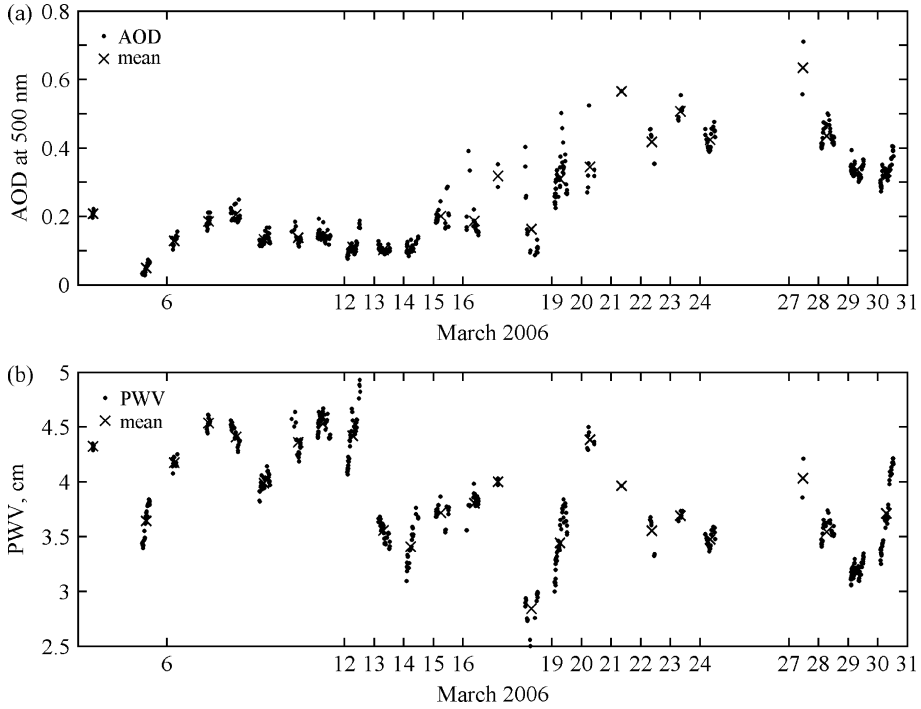

Figure 8. Temporal variation of (a) aerosol optical depth (AOD) at 500 nm and (b) precipitable water vapour (PWV in cm) at MCOH during the MAC experiment. The dates when flights occurred are marked along the *x*-axis.

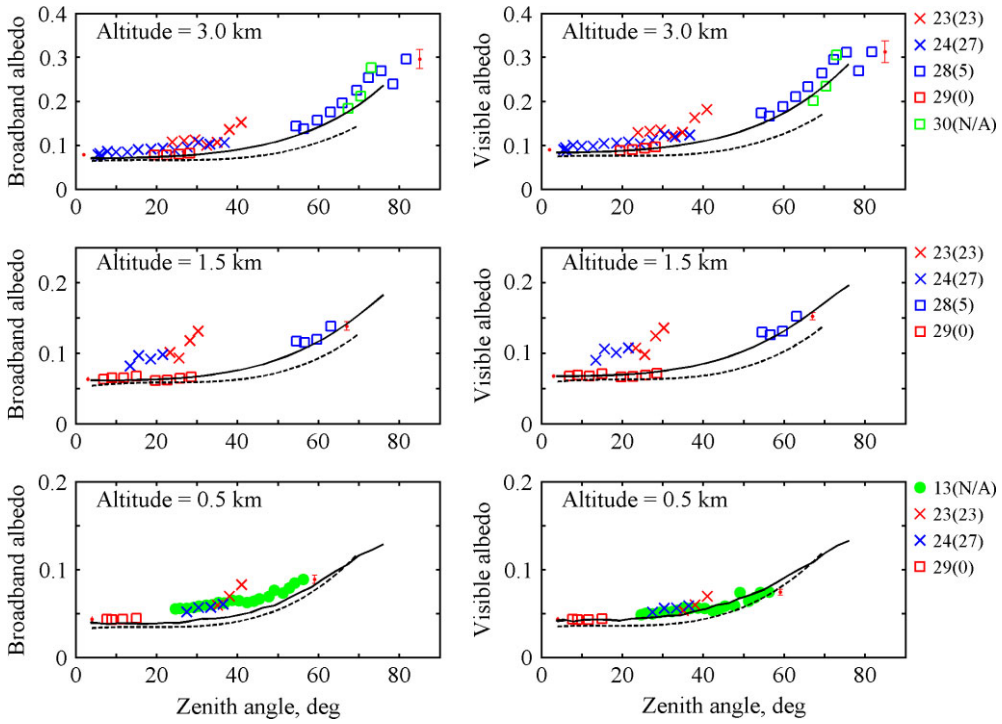

Figure 9. Measured albedos in the broadband (0.3–2.8 μm) and visible (0.4–0.7 μm) region of the solar spectrum as a function of solar zenith angle at 3.0, 1.5 and 0.5 km altitudes for near cloud-free days. Overlaid continuous and dashed lines are theoretically (MACR) calculated albedos on 29 March 2006 for aerosol and aerosol-free atmosphere. The numbers in the bracket along the day number indicates the number of individual cloud elements sampled using IC platform during the respective mission. N/A stands for data not available. For clarity of the figure, error bars are only given for the first and last data points. This figure is available in colour online at www.interscience.wiley.com/qj

DOI: 10.1002/qj

flight period, and as a result the rest of the analyses will pertain to this date.

(1) *Absorption Optical Depth*: A fundamental parameter that governs aerosol solar absorption is the absorption optical depth in visible wavelengths. The column-averaged absorption aerosol optical depth at 520 nm from AERONET was 0.025 whereas the vertically integrated UAV aethalometer (0–3 km) value was 0.019. Thus the remotely sensed aerosol absorption is consistent with the *in situ* observations.

(2) *Albedo at the top of the haze layer*: The measured albedos at 3 km altitude on 29 March in the broadband and visible regions are 0.099 ± 0.008 and 0.119 ± 0.007, respectively. The respective MACR calculated at 3 km altitude are 0.111 ± 0.004 and 0.126 ± 0.004, i.e. within 10% of the measured values.

(3) *Solar absorption*: The absorption is defined as the difference between the net fluxes at two flight levels. The net flux is the difference between the incoming and the outgoing (reflected) fluxes at each altitude. On 29 March, the AC and BC platforms were flown stacked in the same vertical column with different altitude separation, which were at 3.0, 2.6, 2.1, 1.5 km and at 1.5, 1.2, 1.0, 0.5 km a.m.s.l. for the AC and BC platforms, respectively. The data from each platform were averaged over its flight path prior to calculating the net flux. The difference between the averaged net fluxes at different altitudes yielded atmospheric absorption values within the layer separating the platforms. The altitude variations of mean atmospheric absorption in the broadband region (0.3–2.8 μm) for different atmospheric layers are shown in Figure 10(a) for 29 March. In addition, the flux differences and absorption values both measured and calculated are given in Table III. In order to combine flux measurements made at different solar zenith angles, the flux measurements were all normalized to the mean solar zenith angle. In addition to the measurements, the simulated values are shown in Figure 10(a). The calculations were done for both a confined track mean and a domain mean. The two values need not be the same due to spatial variability in the surface albedo. The range of calculated values shows the importance of accounting for the inhomogeneity in sea surface when calculating absorption from observations. MACR-calculated absorption values are within the instrumental uncertainties (7.5 W m^{-2}) of the measured absorption values.

The measured atmospheric absorption values are close to 80 W m^{-2} for layers at higher altitudes (>1.5 km) and are close to 50 W m^{-2} for layers at lower altitudes in the broadband region. These absorption values are compared with those calculated for an aerosol-free atmosphere using the MACR algorithm, which are given in Table III. The differences between the observed absorption and that from the aerosol-free atmosphere are indicative of atmospheric absorption due to aerosols at different altitudes. The aerosol absorption accounted for 30% to 50% of the total absorption depending upon the altitude and solar zenith angle. The significant aerosol absorption was due to a layer of highly absorbing aerosol, black

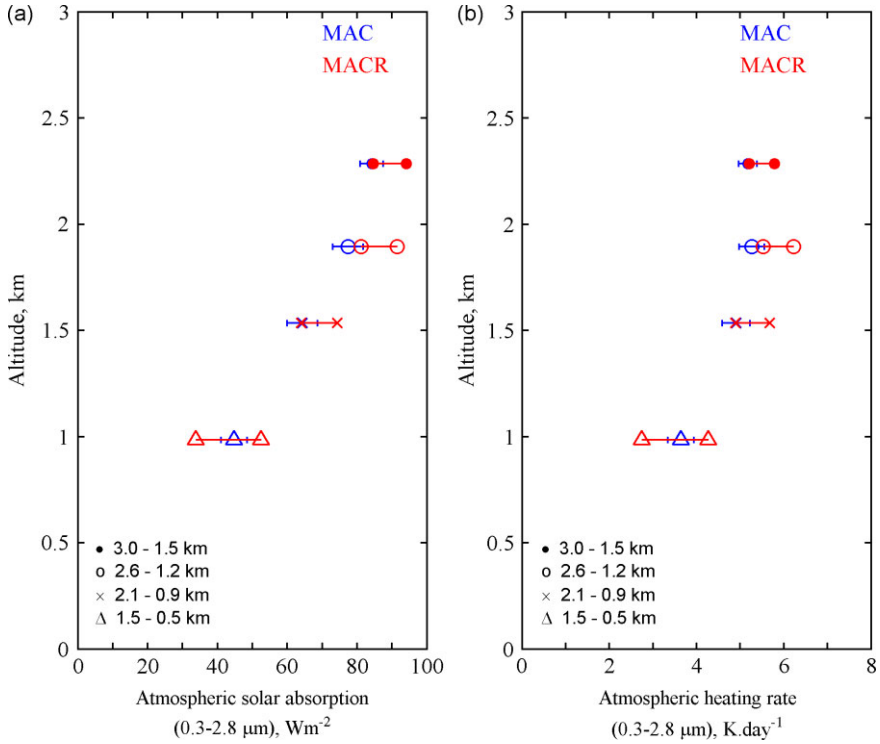

Figure 10. Altitude variation of measured and calculated mean absorption values for different atmospheric layers on 29 March. This figure is available in colour online at www.interscience.wiley.com/qj

DOI: 10.1002/qj

Table III. Comparison of measured and MACR calculated flux differences (incoming as well as reflected flux) and absorption between platform altitudes in the broadband region on 29 March.

Altitude, m	θ_o, deg range	$\Delta F\downarrow$,Wm^{-2} MAC	$\Delta F\downarrow$,Wm^{-2} MACR	$\Delta F\uparrow$,Wm^{-2} MAC	$\Delta F\uparrow$,Wm^{-2} MACR	$A(\Delta F\downarrow - \Delta F\uparrow)$ Wm^{-2}, MAC	A, Wm^{-2} MACR	A-aerosol Wm^{-2}
3050–1520	28–17	107.6 ± 4.6	106.6	23.38 ± 0.8	21.92	84.22 ± 5.11	84.68	59.61
2590–1200	15–8	102.8 ± 5.1	109.9	25.46 ± 0.7	28.75	77.34 ± 5.84	81.15	42.58
2130–940	5–3	89.2 ± 2.6	92.5	24.84 ± 0.6	28.48	64.36 ± 2.83	64.02	34.49
1520–460	7–16	74.8 ± 3.5	63.8	27.87 ± 1.1	30.04	44.73 ± 3.30	33.76	20.46

θ_o: Solar zenith angle; F $\downarrow$: Incoming flux; F $\uparrow$: Reflected flux; $\Delta F\downarrow$: Incoming flux difference; $\Delta F\uparrow$: Reflected flux difference; A: Absorption; A-aerosol: Absorption without aerosols

carbon, that was observed on 29 March between the altitudes 1.5 and 2.5 km.

The solar heating rates calculated from the observed solar absorption in Figure 10(a) are shown in Figure 10(b). The simulated heating rates are also shown in Figure 10(b). The measured instantaneous heating rates are as high as 4–5 K day^{-1} for all layers. Figure 10(a), 10(b) and Table IV show that the simulated absorption and heating rates are within 10% of the observed values for broadband absorption and within 15% for visible absorption. Since aerosols contribute about 90% of the absorption in the visible (compare the MACR case with and without aerosols in Table IV), the visible absorption comparison confirms the treatment of aerosol visible absorption in the model. It also indirectly confirms the UAV-measured values of visible absorption coefficient (by the aethalometer) since the model uses the measured values to estimate the absorption. In summary, the comparison of observations and simulations (Table IV) demonstrates the closure between the measured and simulated atmospheric solar absorption and heating rate. It also suggests strongly that there is no need to introduce 'ad hoc' or 'anomalous' physics into the model.

The large values of observed atmospheric absorption and heating rates are contributed to by the presence of absorbing aerosols (i.e. black carbon) resulting from long-range transport from the sources of pollution. The mean AOD was as much as 0.35 on this day. The vertical profile of aerosols indicated high aerosol concentrations ($\sim$2000 cm^{-3}) between 1.5 and 2.5 km altitude a.m.s.l. over this region. Using MAC data, Corrigan *et al*. (2007) reported high values of $\sim$700 $ng.m^{-3}$ of black carbon concentrations between 1.5 and 2.5 km altitudes on 29 March. The relative importance of aerosol and gaseous absorption is discussed next.

5.4. Physics of atmospheric solar heating

Here we use MACR to quantify the contribution of aerosols and gases to the atmospheric solar heating rates. The results are for diurnal mean heating rates. Absorption results were converted to diurnal mean values. Due to lack of diurnal flux measurements, MACR diurnal flux curves were used to deduce diurnal fluxes from measurements at each altitude. Diurnal mean fluxes were calculated by using the daytime measured fluxes at each altitude fitted to an estimated diurnal flux curve produced with the MACR algorithm.

The diurnal mean broadband solar heating rate (between 0.5 and 3.0 km) obtained from observed values is 1.5 ± 0.3 K/day (Table IV) and the simulated value is 1.6 ($\pm$0.1) K/day. Without aerosols, the simulated value drops to 1.2 K/day. Aerosols accounted for 25% of the broadband heating rates and as much as 90% of the heating rate in the visible region.

MACR was used to estimate the solar heating due to the gases, namely ozone (O_3), oxygen (O_2), carbon dioxide (CO_2), aerosols and water vapour (H_2O), and these estimates are shown in Figure 11 along with the aerosol heating rates. The atmospheric heating rate due to aerosol was an order of magnitude larger than that due to CO_2 and was nearly one-third the absorption by water vapour.

Table IV. Role of aerosols in measuring the atmospheric absorption and heating rates between 0.5 and 3.0 km altitudes on 29 March. The ranges of uncertainty refer to instrumental accuracy.

Spectral range	Absorption, W m^{-2} 0.5–3.0 km			Heating rate, K day^{-1} 0.5–3.0 km		
	MAC	MACR	MACR (without aerosols)	MAC	MACR	MACR (without aerosols)
Broadband (0.3–2.8 μm)	41.5 ± 3.3	45.4 ± 7.5	34.1	1.46 ± 0.12	1.59 ± 0.26	1.19
Visible (0.4–0.7 μm)	8.3 ± 2.1	7.2 ± 2.6	1.2	0.29 ± 0.07	0.25 ± 0.09	0.04

DOI: 10.1002/qj

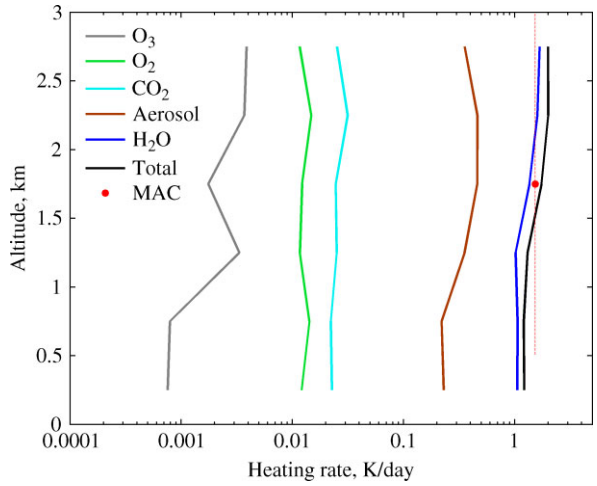

Figure 11. MACR-calculated diurnal atmospheric heating rate profiles from absorbing constituents, namely ozone (O_3), oxygen (O_2), carbon dioxide (CO_2), aerosols, and water vapour (H_2O). The results were calculated using 29 March data for the broadband region. The dot represents the MAC-measured diurnal atmospheric heating rate between 0.5 and 3.0 km altitudes. This figure is available in colour online at www.interscience.wiley.com/qj

6. Conclusions

The Maldives Autonomous UAV Campaign demonstrated the innovative application of stacked AUAVs for resolving outstanding issues such as anomalous solar absorption. The campaign occurred during March 2006 over the tropical Indian Ocean off the coast of the Republic of Maldives. Each UAV was outfitted with miniaturized instruments in order to perform a particular set of measurements. These measurements include aerosol number concentration, aerosol size distribution, aerosol absorption, cloud drop size distribution, cloud liquid water content, solar radiation fluxes (visible and broadband), temperature, pressure and relative humidity. In the stacked three-UAV configuration, UAVs were programmed to pass over the same geographic point (or clouds) within seconds of each other in order to measure aerosol–cloud–radiation parameters within the same column simultaneously. After proper calibration of the instruments and the application of attitude correction procedures, in-flight comparisons between instruments showed agreement within 5 W m^{-2} (<1%) for the incoming fluxes and 3 W m^{-2} (<4%) for the outgoing fluxes.

During the MAC campaign, the northeast monsoon flow carried pollution from the continent over the Arabian Sea. The AODs were low (<0.2) during the beginning of the experiment and increased to 0.5 for the last half of March. The direct measurements of broadband and visible albedos at multiple altitudes established a positive relationship with aerosol concentrations. The visible albedos were slightly higher than broadband albedos at higher (3 km) altitudes, yet the reverse situation occurred at lower altitudes.

A three-dimensional radiative transfer model, MACR, was used to simulate the measured fluxes by inputting observed data. The measured and simulated solar absorption agreed within 5% for altitudes above 1.0 km and the aerosol absorption accounted for 30% to 50% of the total absorption depending upon the altitude and solar zenith angle. The results indicate that there was no need to invoke spurious or anomalous absorption in the model, provided we account for aerosol black carbon. For example, Kato *et al.* (1997), who employed measurements taken as part of the ARM (Atmospheric Radiation Measurements) Program in Oklahoma, found that their radiative transfer model overestimated the observed downward short-wave total (direct plus diffuse) irradiance to the surface by 5% and the downward short-wave diffuse irradiance at the surface by at least 40%. In our study, aerosols reduced the downward solar irradiance by 9% and enhanced the diffuse solar fluxes at the surface by a factor 3 to 10 depending upon the solar zenith angle, AOD, SSA and PWV. Thus the lack of accurate, vertically resolved aerosol data likely may partially explain the discrepancies reported by Kato *et al.* (1997). Since the three UAVs were flown in stacked formation within a horizontal separation of tens of metres and a temporal separation less than ten seconds, MAC was able to explain the observed solar absorption with the state-of-the-art radiation model. Thus when absorbing aerosols are measured and accounted for in models, and when heating rates are measured directly with stacked aircraft, the simulated clear-sky heating rates agree with the observed heating rates and there is no need to invoke significant anomalous or excess absorption in clear skies, in support of the findings of some of the earlier studies (e.g. Cess *et al.*, 1995; Ramanathan *et al.*, 1995).

The diurnally averaged broadband and visible solar absorption between 0.5 and 3.0 km altitudes were 41 ± 3 W m^{-2} and 8 ± 2 W m^{-2} for a cloud-free day. The observed atmospheric solar absorption translated into a diurnal mean heating rate of 1.5 K/day in the broadband region and 0.3 K/day in the visible region between 0.5 and 3.0 km altitudes. The aerosol contribution to the observed atmospheric heating was calculated as 0.36 K.day^{-1} for the broadband region. The atmospheric heating rate (broadband region) due to aerosol over the tropical Indian Ocean was many times larger than that due to CO_2 and about one-third that contributed by water vapour. These results illustrate the fundamental necessity of measuring the aerosol–radiation–cloud parameters simultaneously at multiple altitudes for solar radiation budget studies.

Acknowledgements

Development and miniaturization of UAV instrumentation were funded by the NSF MRI programme and the Vetlesen Foundation. The MAC campaign was funded by NSF, NOAA, NASA and the Vetlesen Foundation. The MCOH was funded by NOAA and the government of Maldives. This research was supported by NOAA under

DOI: 10.1002/qj

the grant NOAA/NA17RJ1231 and by NSF under the grant ATM05-42531. Permission for use of Maldivian airspace and airport facilities was coordinated via the Ministry of Environment, Energy and Water, Government of Maldives. We are grateful to the Hanimaadhoo Island Chief and the people of Hanimaadhoo for their generous hospitality. We also thank H. Nguyen for his help in conducting the MAC. We thank the two anonymous reviewers for their helpful comments and suggestions.

Appendix A. Data Correction Procedure

The radiometer offset was subtracted from each radiation measured value. The radiometer offsets were routinely measured by covering the radiometers with an opaque cover just before and after the science mission (Dutton *et al.*, 2001). This correction was generally a few watts per square metre or less. Only the radiation data that are measured during the straight legs are considered. The radiation data collected during the ascents, descents or turns are not used for the processing. Temperature fluctuations of the pyranometer body (or differential heating of the pyranometer) can produce offset signals. To avoid this problem, the first-leg data after reaching the cruise altitude were not used for processing. Also, the first 10 seconds' data after reaching the cruise altitude after each turn were not considered. The pyranometer body temperature was measured continuously during all the MAC flights. In general, pyranometer body temperature attained the constant value within a few minutes of reaching cruise altitude.

The response of the pyranometer and PAR are very important because the rapid changes in the pitch and roll can cause errors due to slow response of the pyranometer and PAR sensors. The step-change responses of pyranometer and PAR sensors have been experimentally measured by covering and uncovering the instrument with an opaque cover during the clear-sky conditions. The cross symbols in Figure A.1(a) and (b) show the experimental responses of the pyranometer and PAR respectively. The response times of the pyranometer and PAR are 3 s and 1 s, respectively. The respective step-change responses were theoretically estimated and are described as follows:

$$\text{Pyranometer response} = f(t) + \{f(t-1) - f(t)\}\mathrm{e}^{\left(\frac{-(t-1)}{3}\right)} + \{f(t-2) - f(t)\}\mathrm{e}^{\left(\frac{-(t-2)}{3}\right)}, \quad \text{(A1)}$$

$$\text{PAR response} = v(t) + \{v(t-1) - v(t)\}\mathrm{e}^{\left(\frac{-(t-1)}{2}\right)}, \quad \text{(A2)}$$

where $f(t)$, $f(t-1)$, and $f(t-2)$ are the measured broadband fluxes at t, $t-1$ and $t-2$ seconds respectively. Similarly $v(t)$ and $v(t-1)$ are respective visible fluxes at t and $t-1$ seconds. The continuous lines in Figure A.1(a) and (b) are the theoretical response curves obtained using the above equations. The experimental values and theoretically obtained values are nearly identical, which demonstrate that the responses of the pyranometer and PAR are well approximated by the equations. The MAC-measured incoming broadband and visible fluxes are corrected for the instruments' time constants using the above equations.

Pitch and roll movements during the flight cause deviations of the radiometric sensor detection plane from the

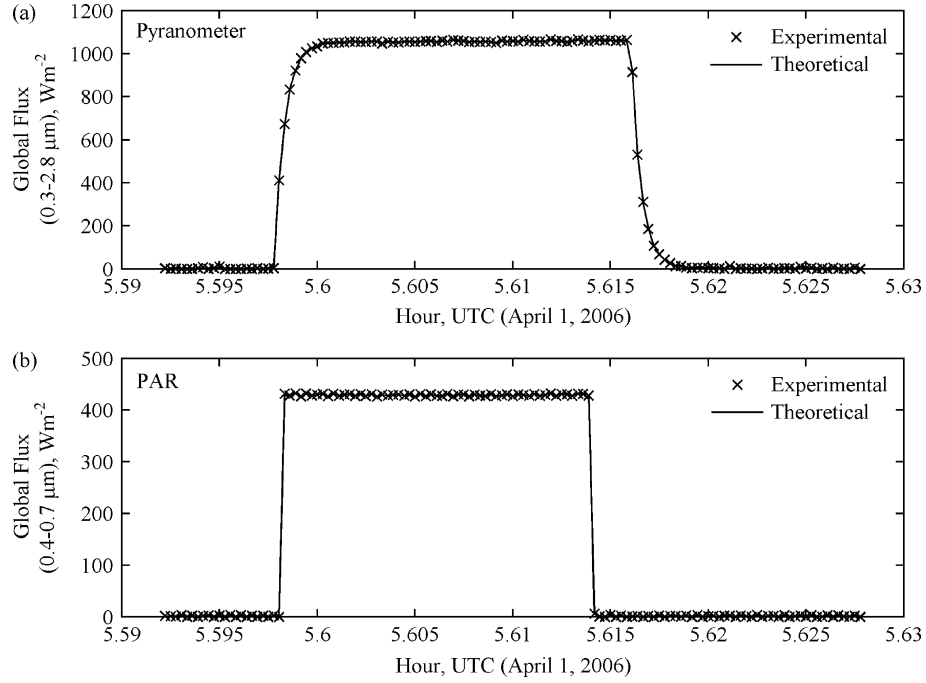

Figure A.1. Response curves of the (a) pyranometer and (b) PAR sensors. The cross symbols represent observed data and the continuous line indicates theoretical values.

DOI: 10.1002/qj

horizontal reference plane of the earth-fixed coordinate frame, which in turn causes the variation in the direct flux on the upward-looking sensors. Whereas this effect is negligible on the reflected flux measurements because the downward-looking (bottom) sensor receives no direct radiation unless the elevation of the Sun is less than the aircraft altitude. Also, this effect is negligible on the diffuse flux since the diffuse flux is isotropic. In addition to the UAV attitude, the offset error due to the mounting of the radiometers in relation to the aircraft navigation system will contribute an additional error to the flux measurements. These mounting offsets (roll and pitch offsets) have been determined for each platform on a day-to-day basis by minimizing the variance of the attitude-corrected normalized radiometric measurements (Saunders *et al*., 1992). The offsets between the inertial navigation system and the radiometric sensors were first determined and then the direct component of the incoming flux was corrected for the non-horizontal orientation of the pyranometer due to UAV pitch (pitch + pitch offset) and roll (roll + roll offset), as described below. The inertial navigation system within the AUAV continuously recorded the pitch, roll, yaw and heading of the aircraft at 1 Hz.

The downward irradiance consists of a direct component and an isotropic diffuse component:

$$G_{z,\theta} = D_{z,\theta} + F_{z,\theta}, \tag{A3}$$

where $G_{z,\theta}$, $D_{z,\theta}$ and $F_{z,\theta}$ are the global flux, direct flux and diffuse flux components respectively at altitude z for a solar zenith angle of θ. The direct component was retrieved from the MAC global flux measurements by making use of direct to global flux ratio, which was obtained from MACR after incorporating the measured aerosol properties into the algorithm (MACR is explained in Appendix B and in Section 3.2).

$$D_{z,\theta} = G_{z,\theta} \times R_{z,\theta}, \tag{A4}$$

where $R_{z,\theta}$ was the MACR-calculated direct to global flux ratio at altitude z for a zenith angle of θ. $G_{z,\theta}$ was the MAC-measured global fluxes. The diffuse component was then retrieved by subtracting the direct flux from the global flux.

$$F_{z,\theta} = G_{z,\theta} - D_{z,\theta} \tag{A5}$$

The mounting offsets (delta pitch and delta roll) were first retrieved by making use of the correction factor ($Cf_{z,\theta}$) that corrects the direct flux data for deviation from level flight from the measurements (Bannehr and Glover, 1991; Saunders *et al*., 1992).

Correction factor

$$Cf_{z,\theta} = A_{z,\theta} \big/ B_{z,\theta}, \tag{A6}$$

where

$$A_{z,\theta} = \sin(\theta_s),$$

$$B_{z,\theta} = \cos(\theta_s)\sin(r)\sin(\varphi - h) - \cos(\theta_s)\sin(p) \times \cos(r)\cos(\varphi - h) + \sin(\theta_s)\cos(p)\cos(r)$$

where θ_s is solar altitude (90° - zenith angle), ψ is azimuth angle of the sun, h is aircraft heading, r is roll angle of the aircraft and p is pitch angle of the aircraft.

The attitude-corrected direct radiation data ($CD_{z,\theta}$) were obtained after applying the correction factor $Cf_{z,\theta}$ to the deduced direct flux data by assuming no installation offsets (i.e. delta pitch (δp) = 0; delta roll (δr) = 0):

$$CD_{z,\theta} = D_{z,\theta} \times Cf_{z,\theta}. \tag{A7}$$

De-trend data were obtained from the corrected direct flux data and the standard deviation of the de-trended data was determined. The delta pitch (δp) was retrieved by searching iteratively for the minimum standard deviation of the de-trend time series, while keeping the delta roll (δr) constant. Using the retrieved delta pitch (δp; new pitch = $p + \delta p$) as a new input parameter, the delta roll (δr) was then determined iteratively. The above iteration scheme was continued until nth and $(n-1)$th iterations yields the delta pitch and delta roll within 0.001°. The retrieved delta pitch and delta roll angles are added to the UAV's inertial navigation system measured pitch and roll angles and thus the obtained correction factor $Cf_{z,\theta}$ is applied to the direct flux. The corrected direct fluxes are then added to the respective diffuse fluxes to yield corrected global fluxes ($CG_{z,\theta}$).

$$CG_{z,\theta} = NCD_{z,\theta} + F_{z,\theta}, \tag{A8}$$

where $NCD_{z,\theta}$ is the attitude- and offset-corrected direct radiation data.

The correction routine is discussed by applying the above procedure to the flux data measured on 24 March at 3 km altitude. Figure A.2(a) and (b) shows the UAV attitude (roll and pitch) variations during an inbound and outbound pair of level tracks on 24 March. The data gaps between the two tracks have been omitted since these correspond to aircraft turns. The roll varied from −6° to +6° and pitch varied from −3° to +2° during the level tracks. Figure A.3(a) is the corresponding correction factor due to only aircraft attitude variations (assumed no offset errors). Figure A.3(b) shows the measured (or uncorrected) and corrected global fluxes for the same two tracks after applying the correction factor shown in Figure A.3(a). The corrected fluxes in Figure A.3(b) indicate the existence of variability in fluxes from track to track even after applying the attitude correction. The correction factor due to aircraft attitude and mounting offset was calculated using the procedure explained above and is shown in Figure B.1(a) for the same two tracks. Figure B.1(b) shows the measured and corrected global fluxes after applying the corrections. The variability of 100 W m^{-2} in the measured fluxes is reduced to less than 20 W m^{-2} after applying the correction. The slight rise in corrected fluxes with time is due to zenith angle changes. The entire MAC radiometer dataset was corrected using the above procedure.

DOI: 10.1002/qj

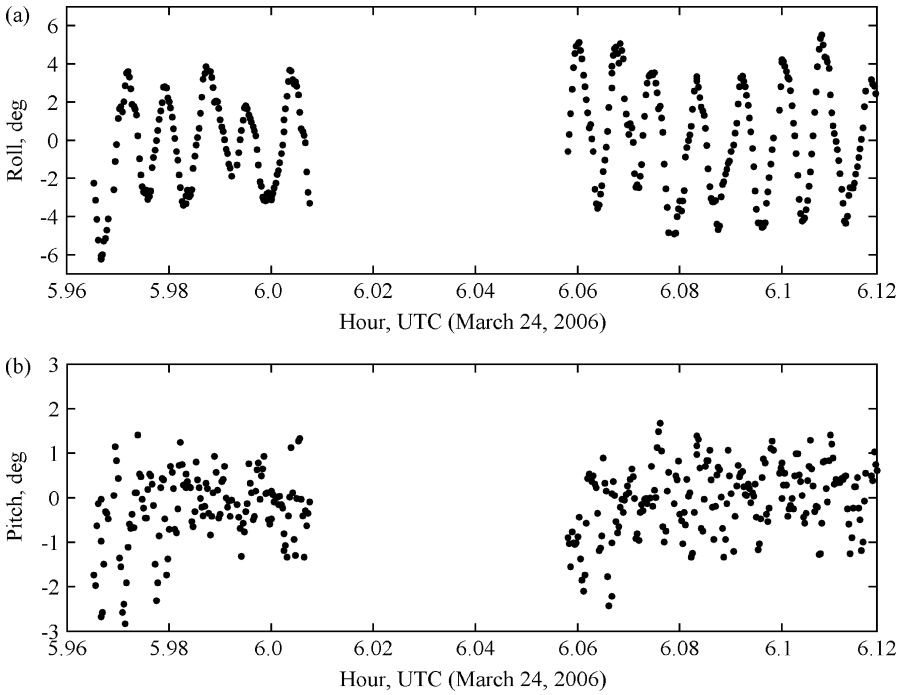

Figure A.2. Variation of UAV pitch and roll during one inbound–outbound cycle on 24 March at 3 km altitude.

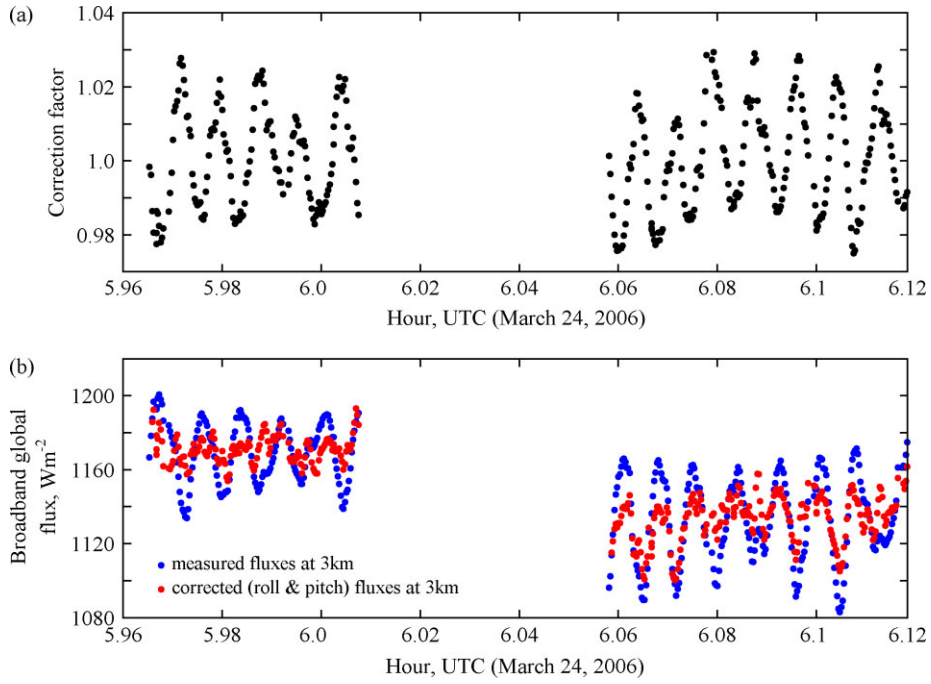

Figure A.3. (a) Correction factor for aircraft attitude pertaining to flight path shown in Figure A.2, and (b) the corresponding measured and corrected fluxes. This figure is available in colour online at www.interscience.wiley.com/qj

Appendix B. Monte-Carlo Radiative Transfer Model

The radiative transfer model used in this study is a clear-sky version of the Center for Clouds, Chemistry, and Climate (C4) three-dimensional broadband Monte-Carlo Aerosol Cloud Radiation model (Podgorny *et al*., 1998, 2000; Podgorny and Ramanathan, 2001; Ramanathan *et al*., 2001; Vogelmann *et al*., 2001).The model uses 25 bands and a total of 3132 pseudo-monochromatic calculations to cover the solar spectrum from 0.25 to 5.0 μm (see Vogelmann *et al*. (2001) for more details). We use two schemes for broadband integration. The first scheme, integration in the visible (0.4–0.7 μm), is used for simulation of measured visible fluxes (incoming and reflected), atmospheric solar absorption and heating rates. The second scheme is applied to the broadband spectrum (0.3–2.8 μm) to simulate the measured broadband fluxes, atmospheric solar absorption and heating rates. Correlated k-distributions (Kato *et al*., 1999) are used to

DOI: 10.1002/qj

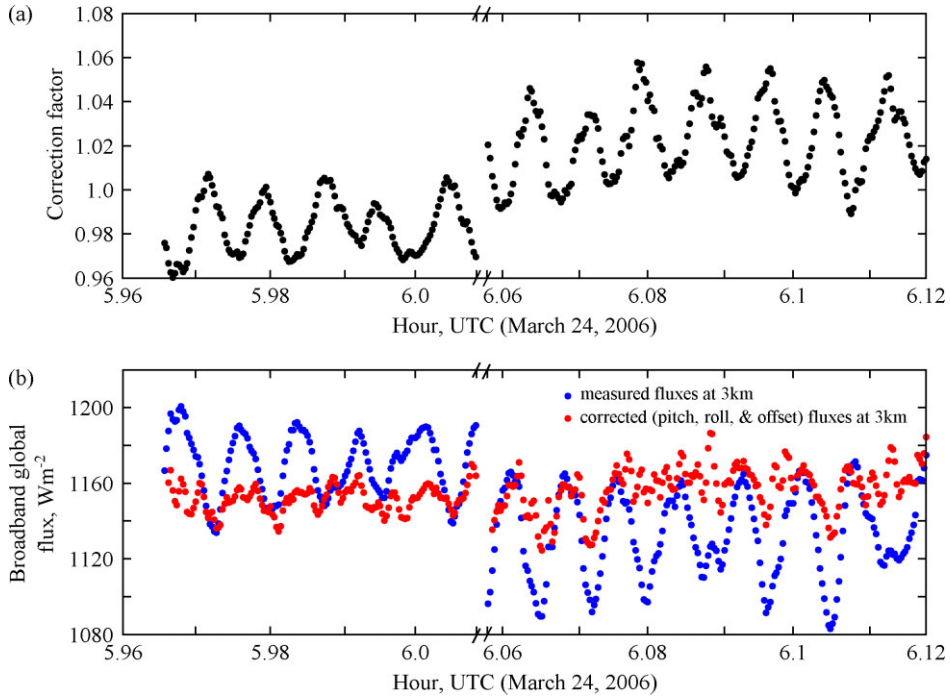

Figure B.1. (a) Correction factor due to aircraft attitude and mounting offsets for the same flight path shown in Figure A.2, and (b) the corresponding measured and corrected fluxes. This figure is available in colour online at www.interscience.wiley.com/qj

incorporate gaseous absorption by water vapour, ozone, oxygen, carbon dioxide etc. (see Vogelmann *et al*. (1998) for more details). The model accounts for all multiple scattering and absorption by individual aerosol species, cloud droplets, air molecules, and reflections from the surface (see Podgorny and Ramanathan, 2001). Scattering angles are computed by a linear interpolation in a table of the inverse cumulative scattering probability (Barkstrom, 1995), so the model assimilates the Mie phase function without compromising angular resolution. The surface albedo is calculated according to Brigleb *et al*. (1986) (see Podgorny *et al*. (2000) for more details). The diurnal time averaging is performed by Monte-Carlo integration over the solar zenith angle. In such a way, time expenses for calculating broadband and diurnal average broadband fluxes are nearly the same. The model profile uses 50 atmospheric layers with a vertical resolution of 0.5 km from the surface to 16 km, 2 km from 16 to 40 km, and 10 km from 40 to 100 km. The top of the atmosphere solar flux is from Kurucz (1992). The measured column-integrated input parameters, namely AOD (0.32), SSA (0.89), asymmetry factor (0.71), water vapour (3.15), ozone (267.1), angstrom exponent of AOD (0.92), and angstrom exponent of SSA (0.07), were used for the MACR calculations. The values given in brackets are specific to 29 March at 0900 UTC (1400h local time); however, simulated fluxes were calculated using temporally relevant data.

References

Ackerman TP, Flynn DM, Marchand RT. 2003. Quantifying the magnitude of anomalous solar absorption. *J. Geophys. Res.* **108**: 4273, DOI: 10.1029/2002JD002674.

Arking A. 1996. Absorption of solar energy in the atmosphere: Discrepancy between model and observations. *Science* **273**: 779–782.

Arking A. 1999. Bringing climate models into agreement with observations of atmospheric absorption. *J. Climate* **12**: 1589–1600.

Asano S, Uchiyama A, Mano Y, Murakami M, Takayama Y. 2000. No evidence for solar absorption anomaly by marine water clouds through collocated aircraft radiation measurements. *J. Geophys. Res.* **105**: 14761–14775.

Bannehr L, Glover V. 1991. 'Preprocessing of airborne pyranometer data.' NCAR Technical Note, NCAR/TN-364+STR, National Center for Atmospheric Research, Boulder, Colorado, USA.

Barkstrom BR. 1995. An efficient algorithm for choosing scattering direction in Monte Carlo work with arbitrary phase functions. *J. Quant. Spectrosc. Radiat. Transfer* **53**: 23–38.

Briegleb BP, Minnis P, Ramanathan V, Harrison E. 1986. Comparison of regional clear-sky albedos inferred from satellite observations and model computations, *J. Appl. Meteorol.* **25**: 214–226.

Cess RD, Zhang MH, Minnis P, Corsetti L, Dutton EG, Forgan BW, Garber DP, Gates WL, Hack JJ, Harrison EF, Jing X, Kiehl JT, Long CN, Morcrette JJ, Potter GL, Ramanathan V, Subasilar B, Whitlock CH, Young DF, Zhou Y. 1995. Absorption of solar radiation by clouds: Observations versus models. *Science* **267**: 496–499.

Cess RD, Zhang M, Valero FPJ, Pope SK, Bucholtz A, Bush B, Zender CS, Vitko J. Jr. 1999. Absorption of solar radiation by the cloudy atmosphere: Further interpretations of collocated aircraft measurements. *J. Geophys. Res.* **104**: 2059–2066.

Corrigan CE, Ramanathan V, Schauer JJ. 2006. Impact of monsoon transitions on the physical and optical properties of aerosols. *J. Geophys. Res.* **111**: D18208, DOI: 10.1029/2005JD006370.

Corrigan CE, Roberts GC, Ramana MV, Kim D, Ramanathan V. 2007. Capturing vertical profiles of aerosols and black carbon over the Indian Ocean using autonomous unmanned aerial vehicles. *Atmos. Chem. Phys. Discuss.* **7**: 11429–11463.

Dubovik O, Smirnov A, Holben BN, King MD, Kaufman YJ, Eck TF, Slutsker I. 2000. Accuracy assessments of aerosol optical properties retrieved from Aerosol Robotic Network (AERONET) Sun and sky radiance measurements. *J. Geophys. Res.* **105**: 9791–9806.

Dutton EG, Michalsky JJ, Stoffel T, Forgan BW, Hickey J, Nelson DW, Alberta TL, Reda I. 2001. Measurement of broadband diffuse solar irradiance using current commercial instrumentation with a correction for thermal offset errors. *J. Atmos. Oceanic Technol.* **18**: 297–314.

Francis PN, Taylor JP, Hignett P, Slingo A. 1997. On the question of enhanced absorption of solar radiation by clouds. *Q. J. R. Meteorol. Soc.* **123**: 419–434.

Fritz S. 1951. Solar radiant energy and its modification by the earth and its atmosphere. Pp. 14–29 in *Compendium of Meteorology*, Malone TF (ed). John Wiley: New York.

Halthore RN, Nemesure S, Schwartz SE, Imre DG, Berk A, Dutton EG, Bergin MH. 1998. Models overestimate diffuse clear-sky surface irradiance: A case for excess atmospheric absorption. *Geophys. Res. Lett.* **25**: 3591–3594.

Holben BN, Eck TF, Slutsker I, Tanre D, Buis JP, Setzer A, Vermote E, Reagan JA, Kaufman YJ, Nakajima T, Lavenu F, Jankowiak I, Smirnov A. 1998. AERONET – A federated instrument network and data archive for aerosol characterization – an overview. *Remote Sensing Environ.* **66**: 1–16.

Jing X, Cess RD. 1998. Comparison of atmospheric clear-sky shortwave radiation models to collocated satellite and surface measurements in Canada. *J. Geophys. Res.* **103**: 28817–28824.

Kato S, Ackerman TP, Clothiaux EE, Mather JH, Mace GG, Wesely ML, Murcray F, Michalsky J. 1997. Uncertainties in modeled and measured clear-sky surface shortwave irradiances. *J. Geophys. Res.* **102**: 25881–25898.

Kato S, Ackerman TP, Mather JH, Clothiaux EE. 1999. The k-distribution method and correlated-k approximation for a shortwave radiative transfer model. *J. Quant. Spectrosc. Radiat. Transfer* **62**: 109–121.

Kiehl JT, Trenberth KE. 1997. Earth's annual global mean energy budget. *Bull. Am. Meteorol. Soc.* **78**: 197–208.

Kurucz RL. 1992. 'Synthetic infrared spectra.' In *Infrared solar physics,* Proc. International Astronomical Union Symposium 154, Rabin DM, Jefferies JT, Lindsey C (eds). Kluwer.

Li Z, Trishchenko AP, Barker HW, Stephens GL, Partain P. 1999. Analyses of Atmospheric Radiation Measurement (ARM) program's Enhanced Shortwave Experiment (ARESE) multiple data sets for studying cloud absorption. *J. Geophys. Res.* **104**: 19127–19134.

McClatchey RA, Fenn RW, Selby JEA, Volz FE, Garing JS. 1971. 'Optical properties of the atmosphere.' Report AFCRL-TR-71-0279, Environ. Res. Pap. 354, Air Force Cambridge Res. Lab., Bedford, Mass., USA.

O'Hirok W, Gautier C. 2003. Absorption of shortwave radiation in a cloudy atmosphere: Observed and theoretical estimates during the second Atmospheric Radiation Measurement Enhanced Shortwave Experiment (ARESE). *J. Geophys. Res.* **108**: 4412, DOI: 10.1029/2002JD002818.

Ohmura A, Gilgen H. 1993. Re-evaluation of the global energy balance. *Geophys. Monogr.* **75**: 93–110.

Oreopoulos L, Marshak A, Cahalan RF. 2003. Consistency of ARESE II cloud absorption estimates and sampling issues. *J. Geophys. Res.* **108**: 4029, DOI: 10.1029/2002JD002243.

Pilewskie P, Valero FPJ. 1995. Direct observations of excess solar absorption by clouds. *Science* **267**: 1626–1629.

Podgorny IA, Ramanathan V. 2001. A modeling study of the direct effect of aerosols over the tropical Indian Ocean. *J. Geophys. Res.* **106**: 24097–24105.

Podgorny IA, Vogelmann AM, Ramanathan V. 1998. Effects of cloud shape and water vapor distribution on solar absorption in the near infrared. *Geophys. Res. Lett.* **25**: 1899–1902.

Podgorny IA, Conant WC, Ramanathan V, Satheesh SK. 2000. Aerosol modulation of atmospheric and surface solar heating over the tropical Indian Ocean. *Tellus B* **52**: 947–958.

Ramana MV, Ramanathan V. 2006. Abrupt transition from natural to anthropogenic aerosol radiative forcing: Observations at the ABC-Maldives Climate Observatory. *J. Geophys. Res.* **111**: D20207, DOI: 10.1029/2006JD007063.

Ramanathan V, Vogelmann AM. 1997. Greenhouse effect, atmospheric solar absorption and the earth's radiation budget: From the Arrhenius–Langley era to the 1990s. *Ambio* **26**: 38–46.

Ramanathan V, Subasilar B, Zhang GJ, Conant WC, Cess RD, Kiehl JT, Grassl H, Shi L. 1995. Warm pool heat budget and shortwave cloud forcing: A missing physics? *Science* **267**: 499–503.

Ramanathan V, Crutzen PJ, Lelieveld J, Mitra AP, Althausen D, Anderson J, Andreae MO, Cantrell W, Cass GR, Chung CE, Clarke AD, Coakley JA, Collins WD, Conant WC, Dulac F, Heintzenberg J, Heymsfield AJ, Holben B, Howell S, Hudson J, Jayaraman A, Kiehl JT, Krishnamurti TN, Lubib D, McFarquhar G, Novakov T, Ogren JA, Podgorny IA, Prather K, Priestley K, Prospero JM, Quinn PK, Rajeev K, Rasch P, Rupert S, Sadourney R, Satheesh SK, Shaw GE, Sheridan P, Valero FPJ. 2001. Indian Ocean experiment: An integrated analysis of the climate forcing and effects of the great Indo-Asian haze. *J. Geophys. Res.* **106**: 28371–28398.

Ramanathan V, Ramana MV, Roberts G, Kim D, Corrigan C, Chung C, Winker D. 2007. Warming trends in Asia amplified by brown cloud solar absorption. *Nature* **448**: 575–578.

Saunders RW, Brogniez G, Buriez JC, Meerkötter R, Wendling P. 1992. A comparison of measured and modeled broadband fluxes from aircraft data during the ICE'89 field experiment. *J. Atmos. Oceanic Technol.* **9**: 391–406.

Stephens GL, Tsay S-C. 1990. On the cloud absorption anomaly. *Q. J. R. Meteorol. Soc.* **116**: 671–704.

Valero FPJ, Cess RD, Zhang M, Pope SK, Bucholtz A, Bush B, Vitko J. Jr. 1997a. Absorption of solar radiation by the cloudy atmosphere: Interpretations of collocated aircraft measurements. *J. Geophys. Res.* **102**: 29917–29927.

Valero FPJ, Bucholtz A, Bush BC, Pope SK, Collins WD, Flatau P, Strawa A, Gore WJY. 1997b. Atmospheric Radiation measurements Enhanced Shortwave Experiment (ARESE): Experimental and data details. *J. Geophys. Res.*, **102**: 29929–29937.

Valero FPJ, Pope SK, Bush BC, Nguyen Q, Marsden D, Cess RD, Simpson-Leitner AS, Bucholtz A, Udelhofen PM. 2003. Absorption of solar radiation by the clear and cloudy atmosphere during the Atmospheric Radiation measurements Enhanced Shortwave Experiments (ARESE) I and II: Observations and models. *J. Geophys. Res.* **108**: 4016, DOI: 10.1029/2001JD001384.

Vogelmann AM, Ramanathan V, Conant WC, Hunter WE. 1998. Observational constraints on non-Lorentzian continuum effects in the near-infrared solar spectrum using ARM ARESE data. *J. Quant. Spectrosc. Radiat. Transfer* **60**: 231–246.

Vogelmann AM, Ramanathan V, Podgorny IA. 2001. Scale dependence of solar heating rates in convective cloud systems with implications to general circulation models. *J. Climate* **14**: 1738–1752.

Wielicki BA, Harrison EF, Cess RD, King MD, Randall DA. 1995. Mission to planet Earth: Role of clouds and radiation in climate. *Bull. Am. Meteorol. Soc.* **76**: 2125–2153.

Zender CS, Bush B, Pope SK, Bucholtz A, Collins WD, Kiehl JT, Valero FPJ, Vitko J. Jr. 1997. Atmospheric absorption during the Atmospheric Radiation Measurement (ARM) Enhanced Shortwave Experiment (ARESE). *J. Geophys. Res.* **102**: 29901–29915.